Journal of Materials Chemistry B

Accepted Manuscript

ROYAL SOCIETY OF CHEMISTRY

www.rsc.org/materialsB

Journal of Materials Chemistry B

ARTICLE

Facile Yolk-shell silica nanoparticles for targeting tumor therapy†

Received 00th January 20xx,
Accepted 00th January 20xx

DOI: 10.1039/x0xx00000x

www.rsc.org/

Liangliang Dai, Qingfeng Zhang, Hao Gu and Kaiyong Cai*

Yolk-shell mesoporous silica nanoparticles (YMSN) were synthesized via a facile approach. The YMSN displayed relatively uniform size, good dispersity and hemocompatibility. The YMSN was further used to construct redox-responsive drug delivery system for targeting tumor therapy, by employing a special rotaxane nanovalve based on Pd as end-capping agent, disulfide bonds as intermediate linker and folic acid as targeting motif. Various characterizations proved that the system had been successfully constructed. A series of biological assays demonstrated that the fabricated YMSN system could be triggered by intracellular glutathione for delivering anticancer drug of doxorubicin hydrochloride (DOX), leading to cell apoptosis *in vitro*. More importantly, the YMSN system displayed great potential for targeted tumor therapy *in vivo,* while with minimal toxic side effects.

1. Introduction

In advanced drug delivery field, high loading capacity, good disparity, large surface area and easy functionalization are essentially important for a promising nanocarrier.[1, 2] Diverse carriers including inorganic nanoparticles, micelles, dendrimers were developed drug delivery. [3-6] Recently, yolk-shell nanoparticles attracted much attention as carriers for drug delivery due to the unique structures, i.e. interior core, interstitial hollow spaces, and permeable outer shell, which not only provides a compartment space for drug loading, but also makes it easy to be tuned with sizes of cores and shells. [7, 8] Yolk-shell nanoparticles were actually a hybrid platform of core-shell and hollow nanoparticles, which significantly extended the applications of classic hollow nanoparticles and core-shell nanoparticles due to above unique features. [7, 9] Thus, yolk-shell nanoparticles were also exploited for applications in the fields of nanoreactors, bio-imaging and catalysis. [10-12]

Yolk-shell nanoparticles demonstrate potential advantage as carriers for drug delivery as follows: firstly, the drug loading capacity of yolk-shell nanoparticles was obviously higher than traditional mesoporous materials, e. g. MCM-41, owing to the their interstitial hollow spaces; [13, 14] secondly, the relatively lower density and larger surface areas than those of mesoporous silica nanoparticles (MSNs) with similar sizes were benefit to drug delivery; [15] thirdly, yolk-shell nanoparticles provides potential convenience for multifunctions of conventional hollow nanoparticles, simply by employing various cores into hollow nanoparticles, e.g., gold nanoparticles / quantum dots as cores for bioimaging, [9, 16] iron nanoparticles as cores for targeting, [11] upconversion nanoparticles as cores for catalysis, etc. [17]

In this study, we intended to employ yolk-shell mesoporous silica nanoparticles (YMSN) as carriers to construct drug delivery system. However, the efficient end-capping of mesopores is essentially important for the successful fabrication of the system. Previously, rotaxane nanovalves (including cucurbit uril, β-cyclodextrins and crown ethers etc.) were extensively used as end-capping agents for sealing meso/macropores of related nanoparticles through non-coordination bonds in drug delivery systems. [18-20] Furthermore, the combination modes of nanovalves could significantly affect the rotaxanation kinetics, stability and so on. Generally, the binding property of metal template rotaxanation via coordination interaction is higher than that of non-coordination. [21] A previous study reported that a Pd template rotaxanation could combine special stalk agent and then form as nanovalve through the coordination bonds. [22] Nevertheless, few studies employed metal template rotaxanation as a mechanized nanovalve to block meso/macroporous nanoparticles in drug delivery systems. [23]

In cancer therapy field, the targeted intracellular drug delivery and stimuli-responsive drug release are essentially important to maximize therapeutic effect of anti-cancer drug against a tumor and minimize toxic side effects. [24] As for targeted intracellular drug delivery, although there is a well-known passive targeting of tumors based on enhanced permeability and retention (EPR) effect, the amount of drug accumulated at tumor site is insufficient to suppress a tumor. During tumor evolution process, the corresponding change of vascular density and interstitial fluid

Key Laboratory of Biorheological Science and Technology, Ministry of Education College of Bioengineering, Chongqing University, Chongqing 400044, P. R. China
E-mail: kaiyong_cai@cqu.edu.cn

† Electronic Supplementary Information (ESI) available: DLS size distributions of nanoparticles, FTIR spectra, HNMR spectra, BET and BJH parameters, Quantification analysis of endocytosis, Flow cytometry analysis of endocytosis and apoptosis, Hemolysis assays, EDS and XPS analysis of distribution of nanoparticles in tumor and major organs, Zeta potentials of nanoparticles. See DOI: 10.1039/x0xx00000x.

pressure of a solid tumor would hinder tissue penetration and convective diffusion of nanoparticles via passive targeting pathway. [25] Meanwhile, potential toxic side effects of a drug delivery system may also occur during the passive targeting.[26] Thus, active targeting for tumor therapy was widely investigated. [25] Folic acid (FA), a well-known tumor targeting motif, mediates endocytosis of a drug delivery nanocarrier via specific receptor-ligand recognition, due to the fact that the FA receptor express little in normal tissues, while highly express in various tumors. [6, 20, 27, 28] Thus, FA was selected as the targeting component in this system. On the other hand, as for stimuli-responsive drug release, the stimuli deriving from tumor microenvironment (biological signals) were considered to the most efficient for triggering drug delivery to achieve maximal therapeutic effect. A previous study confirmed that redox stimulus of glutathione (GSH) was a potential trigger for drug delivery to tumor site. [29] GSH is abundant in cancer cells (2-10 mM), which is approximately 100-1000 times higher than that in body fluid. Furthermore, the level of cytosol GSH in some tumor cells was revealed to be at least four times higher than that in normal cells. [30] Thus, the sharp difference of GSH level between tumor and normal cells was widely exploited to fabricate redox-responsive drug delivery system. [31]

Inspired by above in mind, we designed and fabricated a drug delivery system based on YMSN, which demonstrated great potential for targeting tumor therapy *in vivo*. YMSN were synthesized and further conjugated with stalk agent of 2-((4-hydroxy-3-methoxybenzoic acid) methyl)-6-(bromomethyl) pyridine (HBMP) molecules via disulfide bonds as intermediate linkers, and then specially combined with Pd rotaxanation (PDR) molecules, FA molecules were anchored onto the compound YMSN nanoparticles as targeting motifs, resulting in YMSN-HBMP-PDR-FA (Scheme 1). When the anticancer drug loading YMSN-based system reaches tumor site guided by the targeting motif of FA, the over-expressed GSH in tumor microenvironment could break down the intermediate linker of disulfide bonds, leading to drug release simultaneously. Thus, we hypothesized that the anticancer drug loaded YMSN-HBMP-PDR-FA system could cellular specifically deliver drug in response to GSH to induce cell apoptosis *in vitro* and suppress tumor growth *in vivo*.

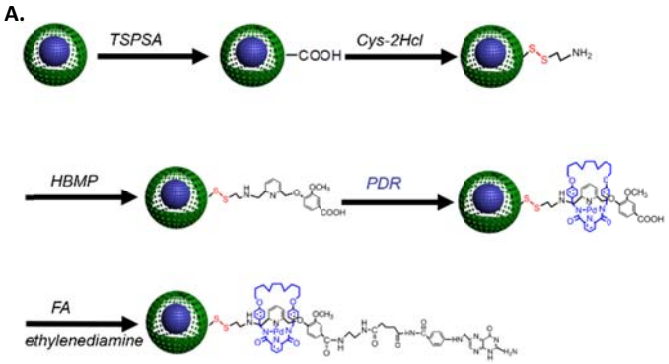

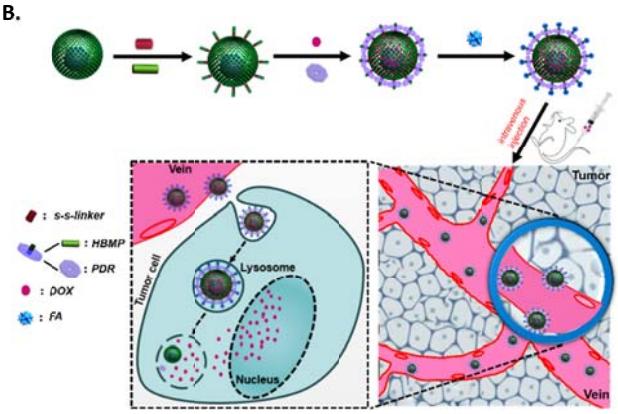

Scheme 1. (A) The fabrication process of YMSN-HBMP-PDR-FA nanocarrier; and (B) targeting tumor therapy of YMSN-HBMP-PDR-FA@DOX system *in vivo*.

2. Experimental section

2.1. Materials

Fluoresceinisothiocynate (FITC), doxorubicin hydrochloride (DOX·HCl), N-hydroxysuccinimide (NHS), tetraethoxysilane (TEOS) and Ethyl-3-(3-dimethylaminopropyl) carbodiimide hydrochloride (EDC·HCl), and were purchased from Sigma-Aldrich (Beijing, China). Folic acid dihydrate (FA), ethylenediamine, cystamine dihyloride and N-cetyltrimethylammonium bromide (CTAB) were supplied by Alfa Aesar (Tianjin, China). 2, 6-bis (Bromomethyl) pyridine, 3-(triethoxysilyl) propylsuccinic anhydride (TSPSA), acetonitrile, N, N-dimethylformamide (DMF) and Dithiothreitol (DTT) were purchased from J&K Scientific Ltd. 2, 6-pyridinedicarbonyl dichloride and palladium acetate were supplied by Heowns Biochem Llc (Tianjin, China). 1, 10-bis [p-aminomethyl) phenoxy] decane and 1, 2-bis (triethoxysilyl) ethane (BTSE) were supplied by Micxy Chemical Co Ltd (Chengdu, China) and Yuhao Chemical Technology Co Ltd (Hangzhou, China), respectively. Triethylamine (TEA), hexane and ethyl acetate were purchased from Chuandong Chemical Co Ltd. (Chongqing, China). Other chemicals were obtained from the Oriental Chemicals Co Ltd. (Chongqing, China). All the reagents were analytical grade.

2.2. Synthesis and functionalization of yolk-shell nanoparticles

The YMSN were synthesized via a surfactant assembly sol-gel process.[8] Briefly, CTAB (0.4163 g) was dissolved into mixture solution containing aqueous ammonia (1 mL, 25 wt %), ethanol (15 mL) and deionized water (52 mL). Then, the above solution was heated to 35 °C, and another mixture solution of BTSE (0.6505 mL) and TEOS (0.6505 mL) was rapidly added with vigorous stirring. After reaction at 35 °C for 24 h, the precipitate was obtained by centrifugation and washed with ethanol for 6 times. Subsequently, the above nanoparticles (500 mg) were dispersed into 80 mL of deionized water and treated at 70 °C for 12 h, and finally collected via centrifugation. To remove the template of CTAB, the crude product was transferred to a mixture solution composed of ethanol (120 mL) and HCl (240 μL, 37 wt %) and stirred at 60 °C for 3 h. The final yolk-shell nanoparticles were obtained by centrifugation and washed with ethanol for 6 times. The samples were dried under

high vacuum (<1000 Pa) for 24 h. The resulting product was denoted as YMSN.

To prepare carboxyl-functionalized YMSN (YMSN-COOH), 1 g of YMSN was dispersed into 100 mL of toluene, and then TSPSA solution (0.814 mL, 2 mM) was dropped into the above solution. The solution was refluxed at 75 °C for 36 h. YMSN-COOH was obtained by centrifugation and washed with methanol for 3 times. The product was dried under high vacuum (<1000 Pa) for 24 h.

The disulfide bond linker YMSN nanoparticles (YMSN-S-S-NH_2) was fabricated according to a previous report.[32] Typically, 0.1 g of YMSN-COOH nanoparticles was dispersed into a mixture solution containing EDC (0.015 M) and NHS (0.015 M) in 20 mL PBS buffer (pH=5) and then 1 g of cystamine dihyloride was added the above solution. The resulting solution was stirred at room temperature for 24 h. The YMSN-S-S-NH_2 were obtained by centrifugation and washed with ethanol and H_2O each for 6 times. The product was then dried under high vacuum for further use.

2.3. Synthesis of 2-((4-Hydroxy-3-methoxybenzoic acid) methyl)-6-(bromomethyl) pyridine (HBMP)

HBMP was synthesized as follows (Figure. S1 A): Briefly, 3-(2-azidoethoxy) phenol (1.67 mmol) was dissolved into acetonitrile solution (10 mL) containing K_2CO_3 (20.1 mmol). After stirring at 60 °C for 20 min, mixture solution containing of 2, 6-bis (bromomethyl) pyridine (5.1 mmol) in acetonitrile (20 mL) was dropwisely added in 10 min and the solution was refluxed with stirring at 60 °C for 24 h. Then, the resulting product was obtained by filtration and then evaporated with reduced pressure. Next, the crude product was purified and obtained a pink solid substance (0.76 mmol, yield = 48.6%) via column chromatography (hexane/ethyl acetate). The obtained product was denoted as HBMP.

2.4. Synthesis of Pd template rotaxane ligand (PDR)

PDR was synthesized according to a previous report (Figure. S1 B).[22] Briefly, 1, 10-bis [paminomethyl) phenoxy] decane (3.725 mmol) was dissolved into anhydrous dichloromethane (500 mL), and then TEA (9.7 mmol) was added to above solution at 0 °C with nitrogen protection. Next, anhydrous dichloromethane solution (20 mL) containing 2, 6-pyridinedicarbonyl dichloride (4 mmol) was dropwisely added at 0 °C within 2 h under nitrogen protection. The solution was then stirred at room temperature for 18 h. The crude product was obtained via reduced pressure treatment and further purified with column chromatography (dichloromethane/ethyl acetate, 1:1) and recrystallized in acetonitrile. The obtained colorless crystal (1 mmol) was then dissolved into anhydrous acetonitrile (15 mL). Next, 0.25 g of palladium acetate (1 mmol) was added to above solution and stirred at room temperature for 1 h under nitrogen protection. The final precipitate was collected via filtration and washed with acetonitrile for 3 times (0.49 g, yield = 78%). The product was dried under high vacuum for further use.

2.5. Fabrication of rotaxane nanovalve-capped yolk-shell drug delivery system

Briefly, 200 mg of YMSN-S-S-NH_2 nanoparticles was dispersed into acetonitrile (50 mL) containing 50 mg of K_2CO_3. Next, the solution of HBMP (200 mg) in acetonitrile (10 mL) was drop wisely added to above solution and refluxed with stirring under at 40 °C for 24 h. The resulting product was collected via centrifugation and washed with deionized water for 6 times until K_2CO_3 was completely removed. Subsequently, the product was washed with acetonitrile and methanol each for 6 times, and dried with lyophilization. The final product was donated as YMSN-HBMP.

DOX and/or FITC were employed as model drugs for the fabrication of drug delivery system. Briefly, 50 mg of YMSN or YMSN-HBMP was dispersed into 50 mL of mixture solution composing of dichloromethane and acetonitrile (8:2, V/V). Then, 15 mg of DOX/FITC were added to above solution and stirred at room temperature for 24 h. The resulting product was obtained via centrifugation. YMSN@DOX/FITC or YMSN-HBMP@DOX/FITC were dried with lyophilization and collected for further experiment.

Finally, 50 mg of YMSN-HBMP nanoparticles was dispersed into a mixture solution composing of PDR (10 mg), dichloromethane and acetonitrile (50 mL, 8:2, V/V). The reaction was lasted with stirring at room temperature for 12 h. The resulting product was collected through centrifugation and washed with dichloromethane for 6 times. The product was dried with lyophilization and named as YMSN-HBMP-PDR. If DOX/FITC was loaded, the product was named as YMSN-HBMP-PDR@DOX/FITC.

2.6. Conjugation of FA to YMSN-HBMP-PDR nanoparticles

YMSN-HBMP-PDR was activated as follows: 100 mg of YMSN-HBMP-PDR nanoparticles, 345.1 mg of EDC and 207.2 mg of NHS were added to 30 mL DMF solution and stirred at ambient temperature for 2 h. Then, 1.67 mL of ethylene diamine was added to the solution and reacted under stirring at ambient temperature for 24 h. The activated product was obtained by centrifugation, washed with DMF and dispersed into 5 mL DMF (Solution 1). Then, the mixture compounds containing 500 mg of FA, 1 g of EDC and 600 mg of NHS were dissolved into 60 mL DMF solution with stirring at ambient temperature for 2 h (Solution 2). Subsequently, solution 1 was added to the solution 2 and stirred for 36 h. The resulting product was collected by centrifugation, washed with DMF for 6 times and dried with lyophilization. The final product was obtained as YMSN-HBMP-PDR-FA. If DOX/FITC was loaded, the product was donated as YMSN-HBMP-PDR-FA@DOX/FITC.

2.7. Material characterization

Morphologies of YMSN and YMSN-HBMP-PDR-FA were characterized by transmission electron microscopy (TEM, LIBRA 200 CS, Carl Zeiss Co., Germany). Emission scanning electron microscopy (FEI Nova 400 Nano SEM, Phillips Co, Holland) equipped with energy dispersive X-ray spectroscopy (EDS) operating at 10 kV or 15 kV was employed for morphology characterization and composition analysis. The surface areas and pore size distributions of various nanoparticles were characterized with Brunauer-Emmett-Teller (BET) and Barrett-Joyner-Halenda (BJH) (ASAP2020M, USA), respectively. Zeta potential measurements (Nano ZS90 Zetasizer, Malvern Instruments Co. Ltd, UK) equipped with dynamic light scattering (DLS), Fourier transforms infrared spectroscopy (FTIR, model 6300, Bio-Rad Co. Ltd., USA), thermal gravimetric analysis (TGA, DTG 60H, Japan), nuclear magnetic resonance spectrometer (NMR, AV500 MHz, Bruker, Swiss) were employed to monitor the series of functionalization procedures. The surface chemistry of the different tissue sections was determined by X-ray photoelectron spectroscopy (XPS) (Model PHI 5400, Perkin Elmer, USA).

2.8. Redox-responsive drug release

Briefly, YMSN-HBMP-PDR-FA@DOX (3 mg) nanoparticles were suspended into 0.75 mL PBS buffer with or without 1 mM and 10 mM GSH or DTT and sealed in a dialysis tube (MWC 8000). The dialysis tube was immersed into 9 mL of PBS buffer solution (pH 7.4) with stirring and incubated at 37 °C. Then, 0.5 mL of supernatant was taken out at given time intervals, and replaced with the same volume of free PBS buffer. The supernatant was analysed by UV/Vis/NIR spectrometer (Lambda 900, PerkinElmer instruments, USA) at a wavelength of 480 nm. The drug loading degree (DLD) and drug loading efficiency (DLE) was calculated from the following equations:

$$\mathrm{DLD}(\%) = \frac{\text{Amount of loaded DOX}}{\text{Total Weight}(\mathrm{YMSN-HBMP-PDR-FA+DOX})} \times 100\%$$

$$\mathrm{DLE}(\%) = \left[1 - \frac{\text{Drug in supernatant liquid}}{\text{Total drug added}}\right] \times 100\%$$

2.9. *In vitro* evaluations

2.9.1 Cell culture. Human hepatocytes (HepG2) and human umbilical vein endothelial cell (HUVEC) were cultured with RPMI1640 medium supplemented and 10 % (v/v) fetal bovine serum (Gibco), 100 μg/mL streptomycin and 100 U/mL of penicillin, under a humid atmosphere containing 5% CO_2 at 37 °C.[33]

2.9.2. Cytotoxicity assay. HepG2 cells were cultured into 24-well plate at an initial cell seeding density of 2×10^4 cells/cm^2. YMSN, YMSN-HBMP-PDR and YMSN-HBMP-PDR-FA nanoparticles were added to each well with a final concentration of 0.286 mg/mL and cultured for 6, 12 and 24 h, when cell confluence reached around 70%. Then the mixture culture medium, which was composed of 20 μL of CCK8 solution and 200 μL of initial medium was added and cultured for another 2 h, and then the solution was measured by a spectrophotometric microplate reader (Bio-Rad 680, USA) at 450 nm. Cell viability was calculated through the value of absorbance and taking the untreated cells as the control.

2.9.3. Morphology visualization. HepG2 cells were seeded at cell density of 10^5/cm^2 and while cell confluence reached around 60-70%. The cells was incubated with YMSN@FITC/DOX and YMSN-HBMP-PDR-FA@FITC/DOX for 6, 12, 24 h, respectively. Next, the cells were washed with PBS and fixed with 4% para-formaldehyde at 4 °C for 0.5 h. The treated cells were stained by DAPI (20 μg/mL), and then washed with PBS for 5 times. Finally, the cells were visualized with CLSM (LSM 510 META Olympus, Japan).

2.9.4. Flow cytometry analysis. Cell apoptosis was detected with an Annexin V-FITC kit purchased from NeoBioscience (China). HepG2 cells were seeded at an initial density of 10^5/cm^2 and incubated with tissue culture polystyrene (TCPS), YMSN, DOX, YMSN@DOX and YMSN-HBMP-PDR-FA@DOX at 37 °C for 24 h during cell confluence reached around 60-70%. After the cells were washed with PBS and collected through centrifugation, the cells were re-suspended in the binding buffer solution with a concentration of 2×10^6 cells/mL. Then, 5 μL of FITC conjugated Annexin V and 10 μL of propidium iodide were added to the cell suspension (195 μL) and incubated at room temperature for 10 min in dark. Finally, 300 μL of supernatant was taken out and analysed using a FACS Calibur (BD Biosciences).

The endocytosis efficiency of YMSN-HBMP-PDR-FA nanoparticles by HepG2 cells and HUVEC cells was also monitor by FACS Calibur. Briefly, when the cells confluence of HepG2 and HUVEC were reached around 60-70%, both cells were incubated with YMSN-HBMP-PDR-FA (0.286 mg/mL) for 2 and 4 h, respectively. The both collected cells were re-suspended in binding solution with a concentration of 5×10^5 cells/mL and analysed using a FACS Calibur.

2.10. *In vivo* evaluations

2.10.1. Establishment of tumor model. All animal experiments were performed based on guidelines of the Institutional Animal Care and Use Committee of China. Male nude mouse of 5 weeks old were supplied from Animal laboratory of Xinqiao Hospital (Chongqing). The tumor-bearing nude mouse model was established through subcutaneously injecting HepG2 cells with a concentration of 5×10^5 cells/ 100 μL PBS at groin one side of each mouse.[29]

2.10.2. *In vivo* tumor therapy. When the tumor volume reached around 50 mm^3, all mice were divided into five groups (5 mice per group) with similar tumor volume and body weights. Nanoparticles and drug (Saline, YMSN, DOX, YMSN@DOX, and YMSN-HBMP-PDR-FA@DOX) were injected into tail vein of mice. The DOX amount was defined as 3 mg/kg/d. The weights of all mice were periodically recorded within 20 days. The tumor size of each mice was recorded via a caliper, and tumor volume was calculated employing the following equation: Tumor volume = $ab^2/2$ (a: the maximum diameter of tumor, b: the minimum diameter of tumor).

2.10.3. Histological assay. The mice were sacrificed after treatments for 20 days. The main organs tissues including tumor, heart, spleen, kidney, lung and liver were separated from all mice and fixed with 10 % formalin for 48 h at 4 °C. Then, those fixed tissues were embedded in paraffin, sectioned and stained with hematoxylin and eosin (H&E). The histological sections were observed with an optical microscope.

2.10.4. TUNEL staining. Tumor sections were treated employing a TUNEL apoptosis detection kit (Beyotime). Firstly, tumor slides were de-paraffinzed and hydrated with dimethylbenzene and ethanol, treated with protease K for 26 min at room temperature, and washed with PBS for several times. Sections were incubated with 50 μL of TUNEL solution in dark for 1 h at 37 °C. Finally, DAPI (20 μg/mL) solution was added and stained for 5 min at room temperature. Sections were observed with CLSM (LSM 510 META Olympus, Japan).

2.11. Statistical analysis

All data were presented as means ± standard deviation (SD). OriginPro (version 8.0) was utilized for statistical analysis. Student's t-test and one-way analysis of variance (ANOVA) was analyzed in this study. The confidence levels of 95% and 99% were regarded as significant difference.

3. Results and discussion

3.1. Synthesis and characterization of YMSN-HBMP-PDR-FA drug delivery system

The YMSN were synthesized via a facile surfactant assembly sol-gel process in this study. As revealed by SEM and TEM images (Figure. 1 A-C), the synthesized YMSN demonstrated round/oval morphology

and good dispersion with distinct feature of interior core, middle hollow space, and permeable outer shell. The multi-step functionalized YMSN-HBMP-PDR-FA nanocontainer displayed similar morphology and structure to YMSN (Figure. 1 D-F vs A-C). Moreover, an unclear shell layer surrounding YMSN was observed (Figure. 1 E-F). The phenomenon could be interpreted that nanovalve and FA molecules were successfully conjugated to YMSN. Besides, dynamic light scattering (DLS) measurements revealed that both YMSN and YMSN-HBMP-PDR-FA had relatively narrow size distributions, with average sizes of 94±5.4 nm and 98±7.2 nm (n=300, Figure. S2).

To systematically reveal the successful fabrication of YMSN-HBMP-PDR-FA system step by step, we employed thermo gravimetric analysis (TGA), brunauer-emmett-teller (BET) and barrett-joyner-halenda (BJH) analysis, zeta potential measurements, Fourier transform infrared spectroscopy (FTIR) and nuclear magnetic resonance (NMR) spectrometer to monitor the functionalization processes. The TGA curves demonstrated a progressive decrease tendency of weight loss corresponding to the consecutive modifications based on YMSN. The result directly suggests that rotaxane nanovalve composing of HBMP and PDR, as well as FA were successfully introduced onto the surfaces of YMSN (Figure. 1 G). Meanwhile, TGA confirmed that around 7.0 wt% of DOX was loaded into YMSN-HBMP-PDR-FA. Moreover, we quantitatively analyzed the drug loading degree (DLD) and drug loading efficiency (DLE), showing the DLD and DLE of the system were 7.18 wt% and 41.27%, respectively.

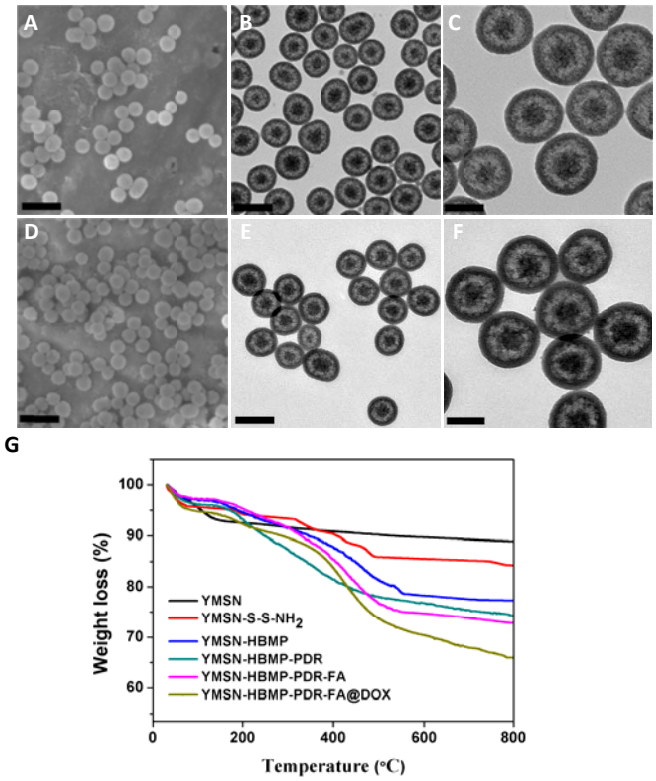

Figure 1. Physical property characterizations: SEM and TEM images of YMSN (A, B) and YMSN-HBMP-PDR-FA (D, E) nanoparticles with corresponding high resolution TEM images (C and F), respectively. Scale bars were 200 nm for A and D, 100 nm for B and E, and 50 nm for C and F, respectively; and (G) TGA curves of various functionalized YMSN nanoparticles.

The curves of BET and BJH displayed a typical type-IV isotherm with a large hysteresis loop (Figure. S3 A), suggesting the mesoporous feature of the materials with a narrow mesopores sizes distribution (Figure. S3 B). [29, 34] The surface areas of YMSN, YMSN-HBMP and YMSN-HBMP-PDR-FA decreased from 877 m^2/g to 158 m^2/g and 69 m^2/g, respectively. Accordingly, the mesopores sizes of nanoparticles also decreased along with the grafting processes (Table S1). Those results imply that rotaxane nanovalve and FA were successfully conjugated to the surfaces of YMSN for end-capping the system. Furthermore, the sequential functionalization process was also confirmed by zeta potential measurement (Figure. S3 C & Table 2). For instance, comparing with that of YMSN-COOH, the charge values of YMSN-S-S-NH_2 shifted from -27.4 mV to 30.3 mV, which was attributed to the introduction of cystamine dihyloride (Cys·2HCl) molecules. More importantly, the zeta potential of YMSN-HBMP-PDR-FA dramatically decreased from -1.4 mV to -15.1 mV when the nanoparticles were exposed to 10 mM GSH for 6 h. It was related to the fact that the linker of disulfide bonds between YMSN and HBMP-PDR-FA were broken down, leading to the exposure of large amounts of negatively charged -SH groups on YMSN. Finally, the FTIR and ^{1}HNMR spectra also detailed suggest that HBMP, PDR and FA molecules were sequentially conjugated to YMSN (Figure. S4 & S5).

3.2. Drug Release Evaluation

An ideal nanocarrier for controlled drug release requires two important features: first, no or limited drug leaking on the way leading for tumor site, a time consuming process, avoiding toxic side effect; second, the drug loading nanocarrier would be triggered by local biological signals for rapid drug release, thus leading to high local drug concentration for killing tumor cells *in vivo*. In this study, we employed UV-vis spectrometer to monitor the drug release profile from YMSN-HBMP-PDR-FA system. First, we investigated the redox responsive drug release behaviour of the system with different stimuli. When exposing to GSH (1 mM and 10 mM) and dithiothreitol (DTT, 10 mM), around 30%, 82% and 90% of DOX released from the system of YMSN-HBMP-PDR-FA@DOX after incubation for 24 h, respectively. While with no stimulus (PBS) applied, only negligible amount (below 10%) of DOX was leaked from the system, indicating good end-capping efficiency of the system (Figure. 2 A). Moreover, compared to GSH (10 mM), DTT (10 mM) triggered more and fast DOX releasing from the system at the initial 5 h, which was consistent with a previous study. [20] It could be contributed to the difference of molecular weights and conformation between DTT and GSH under physiological environment.

Second, to mimic the practical application *in vivo*, we investigated the dynamic drug release behaviour of the system. After incubation for 2 h, the addition of GSH immediately triggered the DOX release from the system of YMSN-HBMP-PDR-FA@DOX (Figure. 2 B), which was ideally mimic the clinic application for tumor therapy. In details, the end-capping of YMSN by Pd-template rotaxane nanovalve efficiently blocked the mesopores of YMSN system, leading to limited leakage on the way to tumor site via

enhanced permeability and retention (EPR) effect or cell targeting. Once the system reaches the tumor site, the over expressed reducing agents (*e.g.* GSH) within tumor microenvironment break down the -S-S- linker of the system, [35, 36] leading to the rapid DOX release from the system for the inhibition of tumor growth.

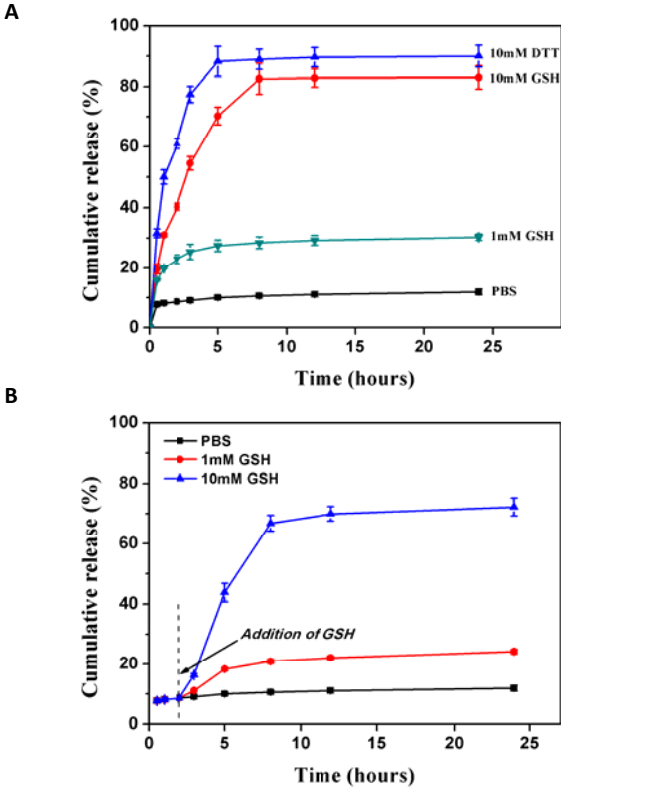

Figure 2. Drug release profiles: (A) redox-responsive release behaviours of YMSN-HBMP-PDR-FA@DOX with various stimuli of DTT and GSH; and (B) dynamic drug release behaviour of the system over 24 h.

3.3. *In vitro* evaluations

To reveal the potential cytotoxicity of YMSN-HBMP-PDR-FA nanoparticles, CCK-8 was used for cell viability assay (Figure. 3 A, a1). The result suggests that the viability of HepG2 cells treated with various nanoparticles (YMSN, YMSN-HBMP-PDR, YMSN-HBMP-PDR-FA) had no difference with that of cells cultured on tissue culture polystyrene plates (TCPS, control) at different time intervals (from 6 h to 48 h), indicating the good cytocompatibility of those nanoparticles. Dose-dependent cytotoxicity assay of YMSN-HBMP-PDR-FA@DOX revealed that low dosage (<0.625 μg/mL) of nanoparticles only led to limited cytotoxicity after co-culture for 48 h, whereas high concentration of nanoparticles (0.625-10 μg/mL) resulted in much severe cytotoxicity than free DOX with same loading concentration ($p<0.01$, Figure. 3 A, a2). The reason could be interpreted that the internalized nanoparticles by HepG2 cells were triggered by intracellular GSH, leading to sustained release of DOX within cells to induce cell death. [32] The result implies that YMSN-HBMP-PDR-FA@DOX system was a promising drug delivery nanocarrier for tumor therapy.

To investigate cellular internalization of various YMSN nanoparticles, we employed TEM and confocal laser scanning microscopy (CLSM) to observe the distributions of within HepG2 cells.[37] Firstly, TEM images showed that HepG2 cells endocytosed YMSN and YMSN-HBMP-PDR-FA had similar cell morphology to that of control (without nanoparticles treatments), showing distinct cell membranes and intact nuclei (Figure. 3 B, dash circles). It was contributed to the good biocompatibility of both nanoparticles (Figure. 3 A, a1). It was also observed that the endocytosis of nanoparticles were firstly distribution in endosome owing to cellular immune response and then enter cytoplasm,[20] and the uptake amount of YMSN-HBMP-PDR-FA much higher than that of YMSN. Interestingly, both endocytosed nanoparticles demonstrated good dispersion within cells' cytoplasm (Figure. 3 B, arrows), which was essentially important for intracellular drug delivery. [38]

Secondly, CLSM images displayed that the endocytosed nanoparticles (YMSN@FITC and YMSN-HBMP-PDR-FA@FITC) were mostly distributed into cytoplasm rather than nuclei, which was in accordance with previous reports. [3, 39] As incubation time extending from 6 h, 12 h to 24 h, the number of endocytosed nanoparticles gradually increased for both nanoparticles (Figure. 3 C). Furthermore, the quantification analysis result was also suggested that the number of endocytosed YMSN-HBMP-PDR-FA@FITC by HepG2 cells was significantly higher ($p<0.01$) than that of YMSN@FITC at each time of interval (Figure. S6). It could be attributed to the FA mediated cell specific endocytosis. [3, 6, 20]

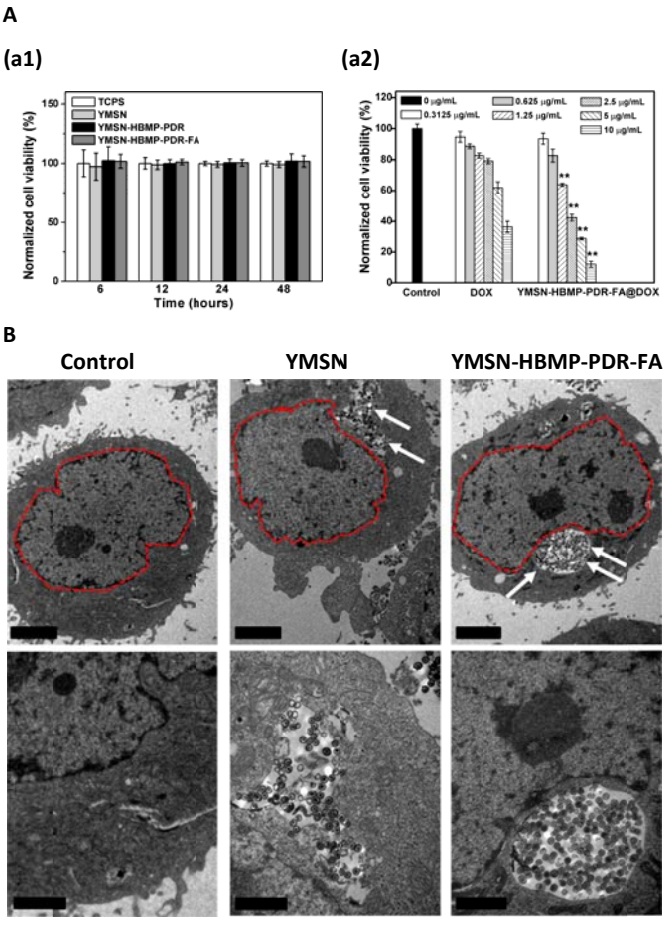

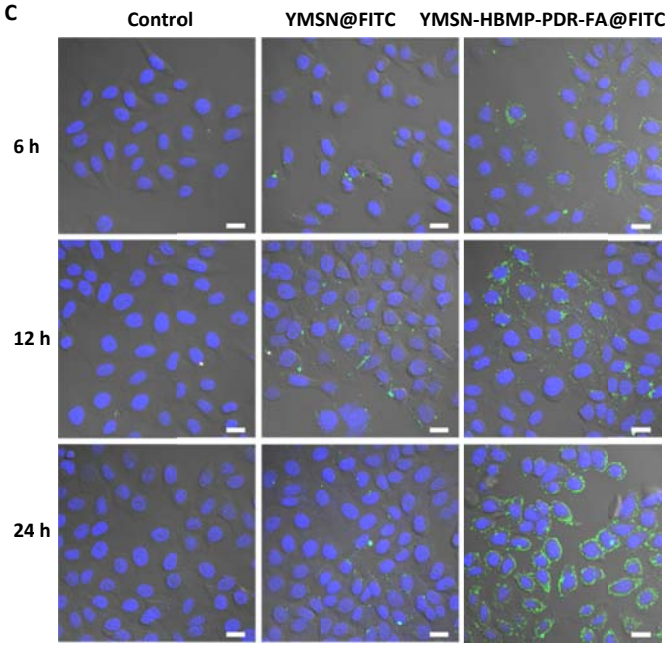

Figure 3. Cytotoxicity and endocytosis assays: (A, a1) Normalized cell viability of HepG2 cells incubated with various YMSN nanoparticles in comparison to control (TCPS) for 6, 12, 24 h, and 48 h, respectively. The normalization was based on the cell viability of TCPS; (A, a2) dose-dependent cytotoxicity of YMSN-HBMP-PDR-FA@DOX system after culture for 48 h; (B) distributions of the endocytosed various nanoparticles within HepG2 cells via TEM observation after culture for 12 h. The concentration of the nanoparticles was 0.286 mg/mL. The lower row images were the enlarged view of upper row images. The scale bars of images in upper row and lower row were 2 μm and 1 μm, respectively; and (C) CLSM images of cells cultured with TCPS, YMSN@FITC and YMSN-HBMP-PDR-FA@FITC for various time intervals. Blue: nuclei, green: nanoparticles. Scale bar: 20 μm. Error bars represent means ± SD (n=4), **p < 0.01.

To reveal the FA mediated cell targeting in details, we firstly blocked the FA receptors on HepG2 cells by pre-incubation with excessive FA (control) before treatment with YMSN-HBMP-PDR-FA@FITC. CLSM images clearly displayed that more fluoresceinisothiocynate (FITC) labelled nanoparticles were uptaken by HepG2 cells that without pre-incubation with free FA than those of control (Figure. 4 A & B). The result directly proved that FA receptor-meditated the endocytosis of YMSN-HBMP-PDR-FA@FITC nanoparticles. Secondly, we employed human umbilical vein endothelial cells (HUVEC) as control to investigate cell specific endocytosis with flow cytometry (FCM). The results again suggest that HepG2 cells endocytosed significantly higher (p<0.01) numbers of FITC labelled nanoparticles than those of HUVEC cells (Figure. 4 C & D). All results indicate that FA receptor over-expressed on the membranes of HepG2 cells mediated cell specific endocytosis of YMSN-HBMP-PDR-FA nanoparticles via a receptor-ligand recognition pathway. [6]

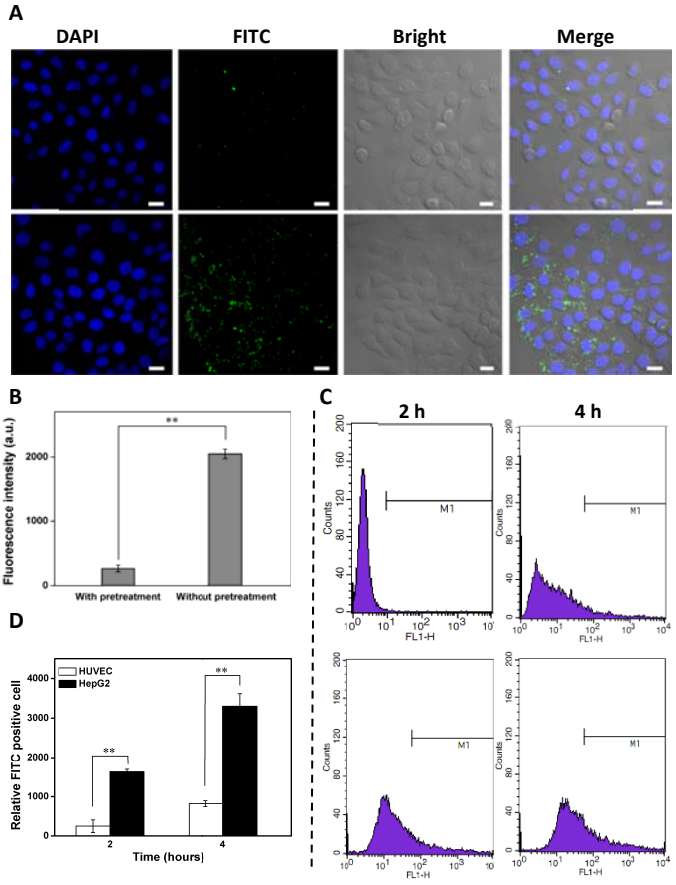

Figure 4. Cell targeting characterization: (A) CLSM images of HepG2 cells pre-incubated with free FA (upper row, 1 mg/mL) or without FA (lower row) and then co-cultured with YMSN-HBMP-PDR-FA@FITC for 24 h. Scale bar: 20 μm; (B) quantitative analysis of fluorescence intensity based on (A); (C) flow cytometry analysis of endocytosis of YMSN-HBMP-PDR-FA@FITC nanoparticles by HUVEC cells (upper row) and HepG2 cells (lower row) after incubation for 2 and 4 h, respectively; and (D) quantification analysis of the endocytosed nanoparticles based on (C). Error bars represent means ± SD (n=4), **p < 0.01.

To evaluate the effect of YMSN-HBMP-PDR-FA@DOX on cell growth *in vitro*, CLSM and FCM was employed to observe cell morphology and quantitatively analyse the apoptosis level of HepG2 cells, respectively. HepG2 cells treated with DOX, YMSN@DOX and YMSN-HBMP-PDR-FA@DOX displayed obvious apoptosis (crushed nuclei) compared to the control (TCPS) (Figure. 5 A). [40] The cell apoptosis in each group became much severe when increasing the incubation time, especially from 12 h to 24 h. Moreover, the apoptosis degree of HepG2 cells caused by YMSN-HBMP-PDR-FA@DOX was obviously severe than YMSN@DOX in spite of incubating time. Furthermore, after HepG2 cells were co-cultured with DOX and DOX loading nanoparticles for 24 h, free DOX was distributed quickly into cell nuclei result from good solubility; YMSN@DOX were distributed into both cytoplasm and cell nuclei due to DOX was immediately release from nanoparticles after incubation with HepG2 cells; while most YMSN-HBMP-PDR-FA@DOX were distributed into cell nuclei, respectively (Figure. 5 B). This results could be interpreted that YMSN-HBMP-PDR-FA@DOX

could be targeted uptake into HepG2 cells with high efficiency and just release DOX triggered by intracellular reducing agents, then the high concentration of DOX accumulation at cells specifically affiliate with DNA and induce severe cell apoptosis / death. [20]

FCM quantification analysis demonstrated that YMSN only induced negligible cell apoptosis/death of HepG2 cells compared to control, again indicating its relatively good biocompatibility. However, DOX, YMSN@DOX and YMSN-HBMP-PDR-FA@DOX induced remarkable cell apoptosis/death with percentage of 13.24%, 12.86%, and 39.26%, respectively (Figure. 5 C & Figure. S7 A). The apoptosis level caused by YMSN-HBMP-PDR-FA@DOX was much higher than those of DOX and YMSN@DOX, which was consistent with above CLSM observation (Figure. 5 A). We further investigated the dose-dependent cell apoptosis induced by YMSN-HBMP-PDR-FA@DOX nanoparticles. The result suggests that the cell apoptosis percentage was directly related to the concentration of nanoparticles (Figure. 5 D & Figure. S7 B), indicating the apoptosis degree was more serious with the increase of concentration of YMSN-HBMP-PDR-FA@DOX ($p<0.01$). The underlying mechanism was listed as follows: first, FA receptor-mediated endocytosis highly improved the uptake efficiency of YMSN-HBMP-PDR-FA@DOX; second, the loaded DOX quickly released from the system within tumor cells triggering by intracellular GSH; third, the relatively high local concentration of DOX accumulating within HepG2 cells induced cell apoptosis / death.

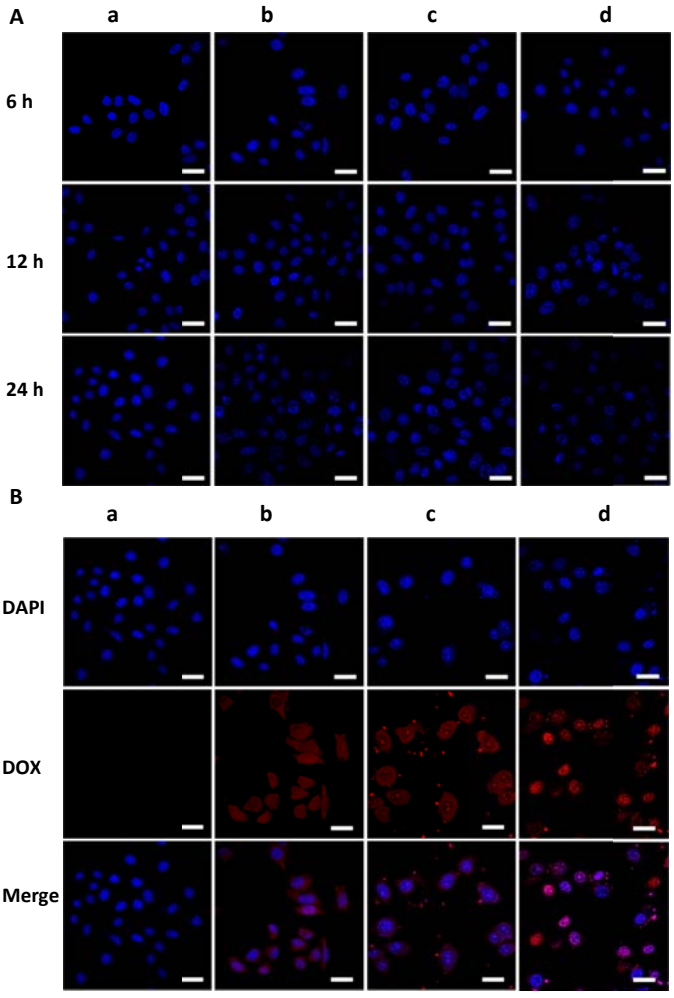

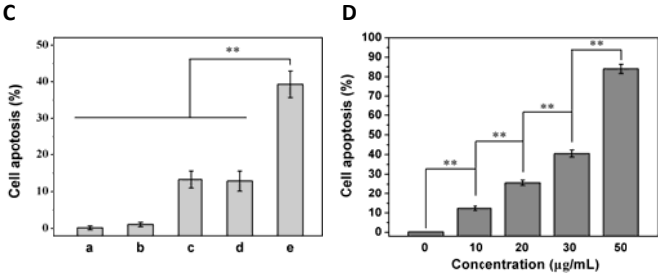

Figure 5. Cell apoptosis assays: (A) representative CLSM images of HepG2 cells cultured with (a) TCPS, (b) DOX, (c) YMSN@DOX and (d) YMSN-HBMP-PDR-FA@DOX (0.286 mg/mL, equal with DOX concentration) for 6, 12, and 24 h, respectively; (B) dual-signal CLSM images of HepG2 cells incubated with above nanoparticles for 24 h. Blue: nuclei, red: DOX. Scale bar: 50 μm; (C) FCM analysis of HepG2 cells apoptosis induced by different treatments with PBS (a, control), YMSN (b), DOX (c), YMSN@DOX (d), YMSN-HBMP-PDR-FA@DOX (e) for 24 h.; and (D) FCM analysis of concentration dependent cell apoptosis induced by YMSN-HBMP-PDR-FA@DOX after culture for 24 h, respectively. Error bars represent means ± SD (n=4), $^{**}p < 0.01$

3.4. *In vivo* evaluations

To investigate the antitumor effect of YMSN-HBMP-PDR-FA@DOX system in details, we firstly constructed a tumor-bearing nude mouse model for further studies in this study. After the mice were intravenously injected with DOX and DOX loading nanoparticles for 20 days, it was observed that the tumor sizes of mice treated with YMSN (positive control) were similar to that of Saline group (negative control); while the tumor sizes of mice treated with DOX and DOX loading nanoparticles were obviously smaller than control groups. YMSN-HBMP-PDR-FA@DOX treated group displayed the smallest tumor sizes among all groups (Figure. 6 A), implying its great potential for suppression of tumor growth.

Next, we periodically measured of tumor volumes and tumor weights during the process of tumor therapy. As for tumor volume, it displayed relatively strong tumor suppression with treatments of DOX, YMSN@DOX and YMSN-HBMP-PDR-FA@DOX when comparing with either negative or positive control groups. More importantly, the YMSN-HBMP-PDR-FA@DOX displayed the most severe ($p<0.01$) tumor growth suppression potential among all groups (Figure. 6 B). The result of tumor weight showed similar tendency (Figure. 6 C). The phenomenon could be explained as follows: as for free DOX group, after DOX was intravenously injected to mice, DOX was rapidly diffused into the whole body via blood circulation. Since DOX has short half-life in blood circulation, [41, 42] only low DOX concentration could be expected at tumor site, thus leading to limited curative effect; as for YMSN@DOX, the carrier could somewhat delay the diffusion of DOX into the host body, thus slightly improving therapy efficiency when compared with that of DOX; while as for YMSN-HBMP-PDR-FA@DOX group, the conjugated FA would improve the endocytosis efficiency of nanoparticles by tumor cells via targeting, leading to the accumulation of YMSN-HBMP-PDR-FA@DOX at tumor site. Next, the system was triggered by intracellular reducing agents such as GSH to locally release DOX in a sustainable manner within tumor tissues, thus resulting in the suppression of tumor growth.

We also monitored the body weights of mice during the therapy process. The result shows that the weights of mice treated with DOX gradually decreased after treatment for 12 days. It could be interpreted that DOX randomly diffused into normal tissues/organs via blood circulation, inducing toxic side effects.[43, 44] Interestingly, the weights of mice gradually increased to 23.6, 23.28, 22.22, 22.64 g after treatment with Saline, YMSN, YMSN@DOX, and YMSN-HBMP-PDR-FA@DOX, respectively (Figure. 6 D). The result implies that YMSN-HBMP-PDR-FA@DOX system could effectively deliver DOX to tumor site for the inhibition of tumor growth, while with only limited side effect *in vivo*, which paving the way for its potential clinic application.

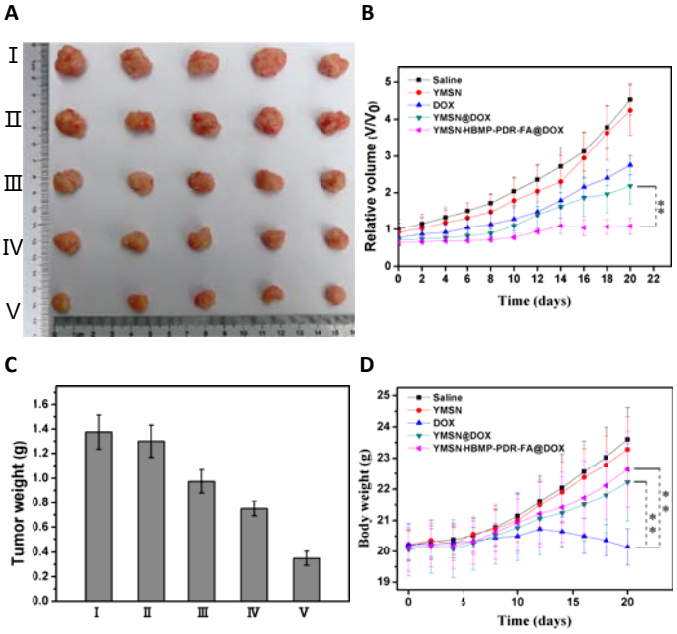

Figure 6. *In vivo* study: (A) representative photos of tumor tissues collected from all treatment groups (Ⅰ: Saline; Ⅱ: YMSN; Ⅲ: DOX; Ⅳ: YMSN@DOX and Ⅴ: YMSN-HBMP-PDR-FA@DOX); (B) Relative tumors volumes and final tumor weights (C) of tumor tissue after treatments for 20 days; (D) Body weight curves of mice subjected to different treatments. The error bars represent mean ± SD (n=5), **p < 0.01.

To further systematically reveal mechanism of the tumor suppression caused by YMSN-HBMP-PDR-FA@DOX system, we performed histological assays. Terminal deoxynucleotidyl transferase dUTP nick end labelling (TUNEL) assay was firstly employed to evaluate the apoptosis of tumor tissue. YMSN induced negligible cell apoptosis in tumor tissues, showing no red dots (labelling apoptosis DNA, Figure. 7 A); DOX and YMSN@DOX induced moderate cell apoptosis in tumor tissues; whereas YMSN-HBMP-PDR-FA@DOX led to most severe cell apoptosis in tumor tissue. Thus, we could draw primary conclusion that DOX locally released from YMSN-HBMP-PDR-FA@DOX system induced cell apoptosis of tumor cells within tumor tissue, in turn inhibiting the tumor growth.

Besides, we employed hematoxylin and eosin (H&E) staining of major tissues to reveal the potential clinical application of the YMSN-HBMP-PDR-FA system (Figure. 7 B). It displayed that YMSN-HBMP-PDR-FA@DOX group caused the most severe damage in tumor than other groups, while no obvious damage to major organs (lung, heart, spleen, liver, and kidney). Moreover, a typical myocardial injury was observed in DOX group, when compared to Saline (control) and YMSN groups.[45] It was contributed to the toxic side effect of free DOX. All results proved that the YMSN-HBMP-PDR-FA@DOX system could cure tumor with high efficiency and significantly decreased the toxic side effect of drug to healthy organs.[46]

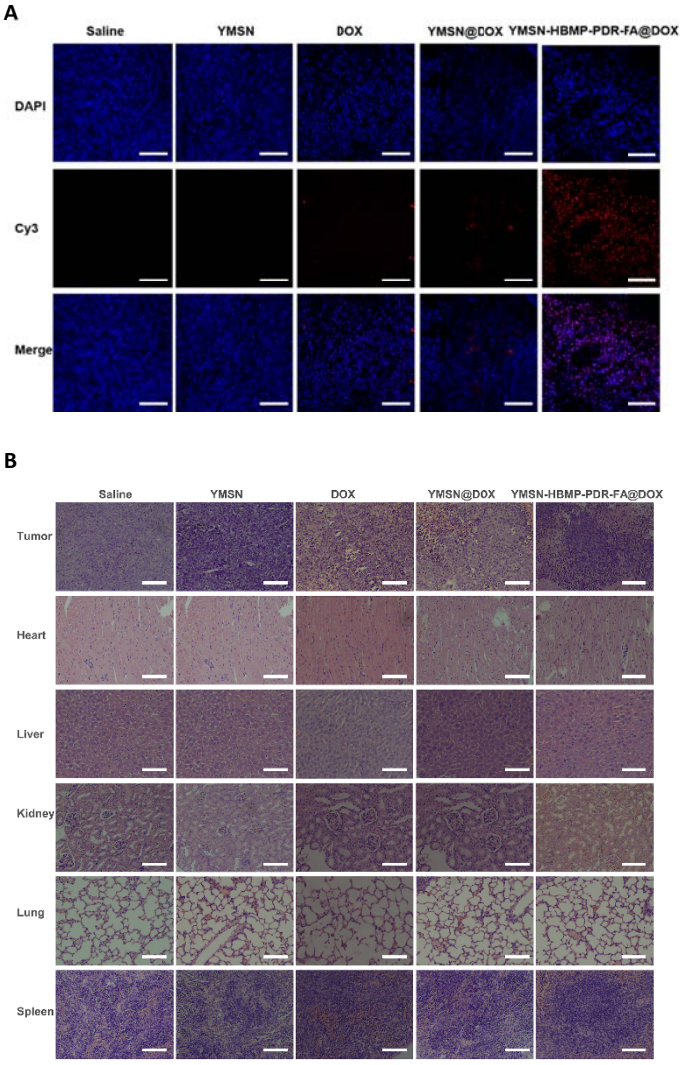

Figure 7. (A) TUNEL staining of tumor tissues subjected to different treatments for 20 days. Blue: cells nuclei; and red: apoptosis DNA. Scale bar: 100μm; and (B) H&E images of tumor and major organs of mice treated with Saline, YMSN, DOX, YMSN@DOX and YMSN-HBMP-PDR-FA@DOX, respectively. Scale bar: 100 μm.

To investigate the biosafety of nanoparticles *in vivo*, energy-dispersive spectrometry (EDS) and X-ray photoelectron spectroscopy (XPS) were used to analyze the distribution of nanoparticles in tumor and major organs, including lung, heart, spleen, liver and kidney. The amount of YMSN-HBMP-PDR-FA@DOX nanoparticles accumulating at tumor tissue was significantly higher ($p<0.01$) than those of others tissues (Figure. S8 & S9). The tumor targeting via over-expression FA receptor and EPR effect improved the endocytosis of YMSN-HBMP-PDR-FA@DOX, leading to the

nanoparticles mostly accumulated at tumor tissues, while less distribution in normal tissues. [47, 48]

Finally, to investigate the hemocompatibility of YMSN-HBMP-PDR-FA carrier for potential clinic application, we comparatively evaluated the hemolysis of human red blood cells (RBCs) (Figure. S10). Herein, solid silica (SiO_2) and MSNs with similar sizes to that of YMSN were selected as negative and positive control, respectively. SiO_2 and MSNs induced around 20% and 76% hemolysis with concentration of 2000 μg/mL; whereas YMSN and YMSN-HBMP-PDR-FA only led to negligible hemolysis with the same concentration. The relatively low acidity and silica density contributed to the good hemocompatibility of YMSN and YMSN-HBMP-PDR-FA, which was consistent with previous reports. [8, 49, 50] The result implies that YMSN-HBMP-PDR-FA was a promising nanocarrier for drug delivery in clinic. Further work by employing YMSN as a platform of multifunctional bioimaging / bioprobe for tumor therapy is under investigation. Taken together, we confirmed our hypothesis that the anticancer drug loaded YMSN-HBMP-PDR-FA system could be trigger by GSH for cellular specifically delivering drug, leading to cell apoptosis *in vitro* and tumor growth inhibition *in vivo*.

4. Conclusions

In summary, we designed and constructed a redox-sensitive drug delivery system based on YMSN with efficient end-capping via Pd-templated rotaxane nanovalve for targeted tumor therapy. Detailed characterizations (TEM, BET, TGA, NMR, etc.) proved that the successful fabrication of the drug delivery system. The subsequent *in vitro* and *in vivo* evaluations demonstrated that the system could be triggered by GSH for delivering DOX, resulting in cell apoptosis and tumor growth inhibition with targeting property. Although further deep investigations need to be performed reveal the feasibility of the system for potential clinical application, the study provides a promising hemocompatible drug delivery vehicle for targeting tumor therapy.

Acknowledgements

Cai gratefully acknowledge the financial support from National Natural Science Foundation of China (21274169 and 31170923), Natural Science Foundation of Chongqing Municipal Government (CSTC, CSTC2013kjrc-ljrcpy0004 and CSTC2013jjB50004), and the “111” project (B06023).

Notes and references

1 X. Du, B. Y. Shi, J. Liang, J. X. Bi, S. Dai, S. Z. Qiao, *Adv. Mater.*, 2013, **25**, 5981-5985.
2 L. Palanikumar, E. S. Choi, J. Y. Cheon, S. H. Joo, J-Y. Ryu, *Adv. Funct. Mater.*, 2015, **25**, 957-965.
3 Z. Luo, K. Y. Cai, Y. Hu, B. L. Zhang, D. W. Xu, *Adv. Healthcare Mater.*, 2012, **1**, 321-325.
4 M. Liong, J. Lu, M. Kovochich, T. Xia, S. G. Ruehm, A. E. Nel, Fu. Tamanoi, J. I. Zink, *ACS Nano*, 2008, **2**, 889-896.
5 M. G. Damiano, R. K. Mutharasan, S. Tripathy, K. M. McMahon, C. S. Thaxtond, *Adv. Drug Deliv. Rev.*, 2013, **65**, 649-662.
6 L. L. Dai, Q. F. Zhang, J. H. Li, X. K. Shen, C. Y. Mu, K. Y. Cai, *ACS Appl Mater Interfaces*., 2015, **7**, 7357-7372.
7 J. Liu, S. Z. Qiao, S. B. Hartono, G. Q. Lu, *Angew. Chem. Int. Ed.*, 2010, **49**, 4981-4985.
8 Z. G. Teng, S. J. Wang, X. D. Su, G. T. Chen, Y. Liu, Z. M. Luo, W. Luo, Y. X. Tang, H. X. Ju, D. Y. Zhao, G. M. Lu, *Adv. Mater.*, 2014, **26**, 3741-3747.
9 C. M. Huang, S. H. Cheng, U. S. Jeng, C. S. Yang, L. W. Lo, *Nano Res.*, 2012, **5**, 654-666.
10 J. Lee, J. C. Park, H. Song, *Adv. Mater.*, 2008, **20**, 1523-1528.
11 H. X. Wu, G. Liu, S. J. Zhang, J. L. Shi, L. X. Zhang, Y. Chen, F. Chen, H. R. Chen, *J. Mater. Chem.*, 2011, **21**, 3037-3045.
12 J. Liu, S. Z. Qiao, J. S. Chen, X. W. Lou, X. R. Xing, G. Q. Lu, *Chem. Commun.*, 2011, **47**, 12578-12591.
13 T. L. Liu, L. L. Lia, X. Teng, X. L. Huang, H. Y. Liu, D. Chen, J. Ren, J. Q. He, F. Q. Tang, *Biomaterials*, 2011, **34**, 1657-1668.
14 Y. F. Zhu, J. L. Shi, W. H. Shen, X. P. Dong, J. W. Feng, M. L. Ruan, Y. S. Li, *Angew. Chem. Int. Ed.*, 2005, **44**, 5083-5087.
15 D. G. He, S. Wang, L. Lei, Z. G. Hou, P. Shang, X. X. He, H. M. Nie, *Chem. Eng. Sci.*, 2015, **125**, 108-120.
16 S. Veeranarayanan, A. C. Poulose, M. S. Mohamed, Y. Nagaoka, S. Iwai, Y. Nakagame, S. Kashiwada, Y. Yoshida, T. Maekawa, D. S. Kumar, *Int. J. Nanomed*, 2012, **7**, 3769-3786.
17 J. J. Peng, L. Z. Zhao, X. J. Zhu, Y. Sun, W. Feng, Y. H. Gao, L. Y. Wang, F. Y. Li, *Biomaterials*, 2013, **34**, 7905-7912.
18 Q. Zhang, F. Liu, K. T. Nguyen, X. Ma, X. J. Wang, B. G. Xing, Y. L. Zhao, *Adv. Funct. Mater.*, 2012, **22**, 5144-5156.
19 J. Pennakalathil, E. Jahja, E. S. Özdemir, Ö. Konu, *Biomacromolecules*, 2014, **15**, 3366-3374.
20 Z. Luo, X. W. Ding, Y. Hu, S. J. Wu, Y. Xiang, Y. F. Zeng, B. L. Zhang, H. Yan, H. C. Zhang, L. L. Zhu, J. J. Liu, J. H. Li, K. Y. Cai, Y. L. Zhao, *ACS Nano*, 2013, **7**, 10271-10284.
21 S. R. Gayam, S. B. Wu, *J. Mater. Chem. B*, 2014, **2**, 7009-7016.
22 D. A. Leigh, P. J. Lusby, A. M. Z. Slawin, D. B. Walker, *Angew. Chem.*, 2005, **117**, 4633-4640.
23 M. Ogawa, A. Kawasaki, Y. Koyama, T. Takata, *Polym. J.*, 2011, **43**, 909-915.
24 S. Mura, J. Nicolas, *Nat. Mater.*, 2013, **12**, 991-1003.
25 V. M. Gaspar, E. C. Costa, J. A. Queiroz, C. Pichon, F. Sousa, I. J. Correia, *Pharm Res.*, 2015, **32**, 562-577.
26 N. Bertrand, J. Wu, X. Y. Xu, N. Kamaly, O. C. Farokhzad, *Adv. Drug Deliv. Rev.*, 2014, **66**, 2-25.
27 J. Sudimack, R. J. Lee, *Adv. Drug Deliv. Rev.*, 2000, **41**, 147-162.
28 X. Ma, Y. Zhao, K. W. Ng, Y. L. Zhao, *Chem. Eur. J.*, 2013, **19**, 15593-15603.
29 L. L. Dai, J. H. Li, B. L. Zhang, J. J. Liu, Z. Luo, K. Y. Cai, *Langmuir*, 2014, **30**, 7867-7877.
30 F. H. Meng, W. E. Hennink, Z. Y. Zhong, *Biomaterials*, 2009, **30**, 2180-2198.
31 A. L. Ortega, S. Mena, J. M. Estrela, *Cancers*, 2011, **3**, 1285-1310.
32 R. Liu, X. Zhao, T. Wu, P. Y. Feng, *J. Am. Chem. Soc.*, 2009, **130**, 14418-14419.
33 K. Y. Cai, Y. Hu, Z. Luo, T. Kong, M. Lai, X. J. Sui, Y. L. Wang, L. Yang, L. H. Deng, *Angew. Chem. Int. Ed.*, 2008, **47**, 7479-7481.
34 A. H. Lu, W. Schmidt, A. Taguchi, H. Spliethoff, B. Thsche, F. Schüth, *Angew. Chem. Int. Ed.*, 2002, **41**, 3489-3492.
35 B. L. Zhang, Z. Luo, J. J. Liu, X. W. Ding, J. H. Li, K. Y. Cai, *J. Control Release.*, 2014, **192**, 192-201.
36 V. Voliani, G. Signore, R. Nifosi, F. Ricci, S. Luin, F. Beltram, *Nanomedicine*, 2012, **2**, 34-44.
37 K. Y. Cai, Y. H. Hou, Y. Hu, L. Zhao, Z. Luo, Y. S. Shi, M. Lai, W. H. Yang, P. Liu, *Small*, 2011, **7**, 3026-3031.

38 A. M. Schrand, J. J. Schlager, L. M. Dai, S. M. Hussain, *Nat. Protoc*., 2010, **5**, 744-757.
39 F. Danhier, O. Feron, V. Préat, *J. Control Release.*, 2010, **148**, 135-146.
40 Z. Luo, K. Y. Cai, Y. Hu, L. Zhao, P. Liu, L. Duan, W. H. Yang, *Angew. Chem. Int. Ed*., 2011, **50**, 640-643.
41 H. Kim, S. Kim, C. Park, H. Lee, H. J. Park, C. Kim, *Adv. Mater.*, 2010, **22**, 4280-4283.
42 S. Dhar, N. Kolishetti, J. S. Lippard, C. O. Farokhzad, *Proc. Natl. Acad. Sci. U.S.A.*, 2011, **108**, 1850-1855.
43 D. Peer, J. M. Karp, S. Hong, O. C. Farokhzad, R. Margalit, *Nat. Nanotechnol*., 2007, **2**, 751-760.
44 H. Meng, M. Xue, T. Xia, Z. X. Ji, D. Y. Tarn, J. I. Zink, A. E. Nel, *ACS Nano*, 2011, **5**, 4131-4144.
45 H. Sah, L. A. Thoma, H. R. Desu, E. Sah, G. C. Wood, *Int J Nanomedicine*, 2013, **8**, 747-765.
46 X. W. Liu, C. C. Chua, J. P. Gao, Z. Y. Chen, C. L. C. Landy, R. Hamdy, B. H. L. Chua, *Am. J. Physiol. Heart Circ. Physiol*., 2004, **286**, H933-H939.
47 D. R. Kalaria, G. Sharma, V. Beniwal, M. N. V. Ravi Kumar, *Pharm. Res.*, 2009, **26**, 492-501.
48 K. Cho, X. Wang, S. M. Nie, Z. D. Chen, M. Shin, *Clin. Cancer Res.*, 2008, **14**, 1310-1316.
49 Y. S. Lin, C. L. Haynes, *J. Am. Chem. Soc*., 2010, **132**, 4834-4842.
50 T. Yu, A. Malugin, H. Ghandehari, *ACS Nano*, 2011, **5**, 5717-5728.

Entry for the Table of Contents

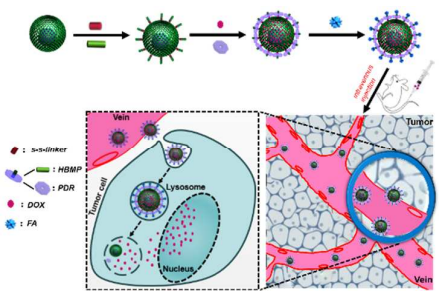

Redox-responsive yolk-shell silica nanoparticles end-capping with rotaxane nanovalves is fabricated for targeting tumor therapy with high efficiency.